INORGANIC CHEMISTRY FRONTIERS

RESEARCH ARTICLE

View Article Online
View Journal | View Issue



Cite this: *Inorg. Chem. Front.*, 2025, **12**, 8148

# Magnetic dynamics and exchange coupling in dinuclear lanthanide complexes bridged by naphthoquinone and anthraquinone radicals

Dimitris I. Alexandropoulos, *[a,b] Kuduva R. Vignesh, [a,c] Luís Cunha-Silva [d] and Kim R. Dunbar *[a]

The use of the bis(bidentate) quinoid ligands 5,8-dihydroxy-1,4-naphthoquinone ($dhnqH_2$) and 1,5-dihydroxyanthraquinone ($dhaqH_2$) in Ln chemistry has afforded four new dinuclear $Dy^{III}$ complexes, *viz.*, $[Dy_2(dhnq)(Tp)_4]$ (**1**), $[Dy_2(dhaq)(Tp)_4]$ (**2**), $\{K(18\text{-crown-6})\}[Dy_2(dhnq)(Tp)_4]$ (**3**) and $\{K(18\text{-crown-6})\}[Dy_2(dhaq)(Tp)_4]$ (**4**) (Tp = tris(pyrazolyl)borate). In compounds **1** and **2**, the $Dy^{III}$ ions are bridged by the diamagnetic dianionic forms of $dhnq^{2-}$ and $dhaq^{2}$, while complexes **3** and **4** are bridged by the one-electron reduced, radical forms of these ligands. The presence of the ligand-centered radical has been confirmed by X-ray crystallography and SQUID magnetometry. Alternating current (ac) magnetic susceptibility studies revealed that the relaxation dynamics of **1** and **2** are primarily governed by fast quantum tunneling of magnetization (QTM). Conversely, the radical-bridged complexes **3** and **4** behave as single molecule magnets (SMMs) with energy barriers for the magnetization reversal, $U_{eff}$, of 24.17 K and 16.70 K, respectively, in the absence of a direct current (dc) applied field. The strong ferromagnetic Dy–radical interactions, computed using *ab initio* POLY_ANISO calculations, led to coupling constants of $J$ = +5.0 and +1.2 $cm^{-1}$ for **3** and **4**, respectively, which explains the SMM behavior in these complexes.

Received 12th July 2025,
Accepted 27th August 2025

DOI: 10.1039/d5qi01477h

rsc.li/frontiers-inorganic



## Introduction

Single Molecule Magnets (SMMs) are discrete species that exhibit magnetic hysteresis of the pure molecular origin and an effective energy barrier ($U_{eff}$) to reversal of the magnetization.[1–4] Apart from their electronic structures, which have been extensively studied over the past several decades, the electron-transport properties of these materials are also of paramount interest for many potential technological applications, including high-density data storage,[5] molecular electronic devices,[6] and quantum computation.[7] The syntheses of these materials often rely on self-assembly reactions between paramagnetic metal ions and organic bridging ligands. Lanthanide ions, in particular $Dy^{III}$ and $Tb^{III}$,[8–11] possess remarkably large single-ion anisotropies compared to other paramagnetic ions of the periodic table, attributes that have been highly successful for the design of new SMMs. Indeed, the first Ln SMM was reported in 2003[12] and since then, a variety of mononuclear[13–20] and polynuclear[11,21,22] 4f metal SMMs have been characterized.

Despite the remarkable progress that has been made in the area of lanthanide metal SMMs, some challenges remain, particularly in the case of polynuclear complexes. Typically, the origin of the magnetic relaxation of these systems arises from the presence of dominant single ion effects rather than the result of a unified spin ground state. This situation is due to the poor radial extension of the 4f orbitals, which limits orbital overlap with bridging ligands, the result of which is weak magnetic exchange.[4] In addition, the majority of bridging ligands that have been used are closed-shell ligands that promote very weak interactions between 4f metal ions and favour fast relaxation processes or quantum tunnelling of the magnetization (QTM). To overcome this limitation, the metal-radical approach[23] has been pursued, which makes use of open-shell bridging ligands with diffuse spin orbitals that can penetrate the core electron density of the lanthanide ions and achieve strong direct coupling.[24–27] Over the last 10 years, considerable effort has been directed at the synthesis of radical-bridged lanthanide complexes with a focus on dinuclear compounds. Indeed, a small but growing number of interesting

[a]*Department of Chemistry, Texas A&M University, College Station, Texas 77842-3012, USA. E-mail: dunbar@chem.tamu.edu*
[b]*Department of Chemistry, University of Patras, Patras 26504, Greece. E-mail: dimalexandrop@upatras.gr*
[c]*Department of Chemical Sciences, Indian Institute of Science Education and Research (IISER) Mohali, Sector-81, Knowledge city, S.A.S. Nagar, Mohali-140306, Punjab, India*
[d]*LAQV/REQUIMTE & Department of Chemistry and Biochemistry, Faculty of Sciences, University of Porto, 4169-007 Porto, Portugal*

dinuclear SMMs have been reported,[24,27] including the remarkable compound $[K(18\text{-crown-6})(THF)_2][\{[(Me_3Si)_2N]_2(THF)Ln\}_2(\mu\text{–}\eta^2\text{:}\eta^2\text{-}N_2)]$ which exhibits magnetic hysteresis up to 14 K.[28]

Following the landmark discovery that the $N_2^{3\bullet-}$ radical can strongly couple two $Ln^{III}$ centers, attention has shifted toward identifying organic radicals capable of achieving similarly efficient magnetic exchange. A key determinant in this context is the nature of the radical ligand, specifically, the number of atoms over which the unpaired electron is delocalized and the degree of metal-radical overlap. Numerous N-donor radical ligands have since been explored, including bipyrimidyl (bpym),[29] tetrapyridylpyrazine (tppz),[30] bisbenzimidazole (Bbim),[31] hexaazatrinaphthylene (HAN),[32] nitronyl nitroxides,[27] indigo,[33] triazinyl, and tetrazine.[34,35] In this vein, our group has focused on developing lanthanide complexes featuring the radical form of the tetrazine-based ligand 3,6-bis(pyridyl)-1,2,4,5-tetrazine (bptz). Using this ligand in 4f metal chemistry afforded a dimetallic radical-bridged complex, $[Cp_2Co][[Dy(tmhd)_3]_2(bptz^{\bullet-})]$ (tmhd = 2,2,6,6-tetramethyl-3,5-heptanedionate),[36] and a supramolecular metallacyclic triangle, $[Dy_3(hfac)_6(bptz^{\bullet-})_3]$ (hfac = 1,1,1,5,5,5-hexafluoro-2,4-pentanedionate).[37]

While N-donor radicals have dominated the field, O-donor radical ligands remain significantly underexplored. Bis(bidentate) benzoquinoids are a well-known category of organic molecules that undergo redox reactions to generate semiquinoid radicals, which have been successfully employed for the synthesis of many radical-bridged metal complexes. These ligands exhibit rich electronic versatility since they can accommodate a variety of donor atoms, including N, O, and S,[38–40] and non-donor atoms or substituents such as Cl, Br, OMe, $NO_2$, and $SMe_2$;[41–43] hence, a wide variety of magnetostructural correlations are rendered possible. Indeed, a number of 3d semiquinoid radical-bridged metal complexes have been reported, ranging from discrete dinuclear compounds[44–49] to extended chains[50] and multidimensional frameworks.[51] In 4f chemistry, $Ln_2$ radical-bridged compounds have been reported, bearing the dichloro- and dibromo-2,5-dihydroxy-1,4-benzoquinone radical derivatives.[41,42]

Motivated by these insights and building on our previous research in radical bridged complexes,[36,37,52–55] we decided to extend this work to relatively unexplored bulkier bis(bidentate) quinoid molecules, namely 5,8-dihydroxy-1,4-naphthoquinone ($dhnqH_2$) and 1,5-dihydroxyanthraquinone ($dhaqH_2$) (Scheme 1), to ascertain if the addition of extra aromatic rings on the semiquinoid radical scaffold affects the strength of metal-radical coupling and the SMM behaviour of the resulting compounds. Although the bridging capabilities and redox activity of these ligands were explored in complexes with heavier d-block metal ions, there is currently no crystallographic evidence of the radical form of these organic molecules.[56–59]

Herein, we report the syntheses, crystal structures, magnetic properties, and theoretical studies of two dinuclear $Dy^{III}$ complexes $[Dy_2(dhnq)(Tp)_4]\cdot 6CH_2Cl_2$ (**1**·$6CH_2Cl_2$) and $[Dy_2(dhaq)(Tp)_4]\cdot 6CH_2Cl_2$ (**2**·$6CH_2Cl_2$), and their radical-bridged analogues $\{K(18\text{-crown-6})\}[Dy_2(dhnq)(Tp)_4]\cdot 2THF$ (**3**·2THF) and $\{K(18\text{-crown-6})\}[Dy_2(dhaq)(Tp)_4]\cdot 2THF$ (**4**·2THF). These results constitute rare examples of O-donor radical-bridged $Dy_2$ complexes and the first examples of structurally characterized metal complexes bridged by a naphthoquinone or an anthraquinone radical.

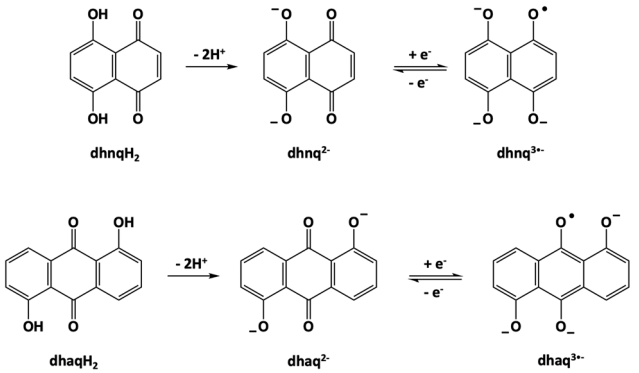


**Scheme 1** Redox states of the ligands used in this work.

## Results and discussion

### Synthetic comments and description of structures

Complexes **1** and **2** were synthesised by reacting $DyCl_3\cdot 6H_2O$, $LH_2$ (L = $dhnq^{2-}$ and $dhnq^{2-}$), KTp, and NaOH in a 2 : 1 : 4 : 2 molar ratio in EtOH. The solvent was removed *in vacuo*, the remaining solid was redissolved in $CH_2Cl_2$, and the resulting solution was left undisturbed for a day, which afforded crystallographically suitable crystals of $[Dy_2(L)(Tp)_4]$ [L = $dhnq^{2-}$ (**1**) and $dhaq^{2-}$ (**2**)] in 75–85% yields.

Compounds **1** and **2** crystallize in the triclinic space group $P\bar{1}$. Both structures (Fig. 1) feature two crystallographically equivalent $[Dy(Tp)_2]^+$ moieties linked together *via* a doubly deprotonated bridging $dhnq^{2-}$ or $dhaq^{2-}$ ligand for **1** and **2**, respectively, with a site of inversion located at the center of the ligand. Each $Dy^{III}$ ion is 8-coordinate, exhibiting a $\{N_6O_2\}$ coordination sphere; six coordination sites are occupied by the N atoms of two capping Tp groups, with the remaining two positions being occupied by the O atoms of the bridging ligand. The $[Dy(Tp)_2]^+$ moiety exhibits a bent sandwich-type architecture with a B–Dy–B angle of 125.0° in **1** and 128.3° in **2**. The bridging $dhnq^{2-}$ and $dhaq^{2-}$ ligands adopt a bis-bidentate binding mode, forming two six-member chelating rings with the metal ions with bite angles of 72.9° and 73.0° and bite distances of the six-member chelate ring of 2.693 Å and 2.698 Å, for **1** and **2**, respectively. Within the bridging ligands, the average C–O bond distances are 1.2853 Å and 1.272 Å in **1** and **2**, respectively, consistent with reported values for the doubly deprotonated diamagnetic form of $dhnq^{2-}$ and $dhaq^{2-}$ in coordination compounds with 4d metal ions.[56–59] The average Dy–O and Dy–N bond distances are similar in both compounds (2.267 Å and 2.514 Å in **1**, and 2.267 Å and 2.508 Å in **2**). The coordination geometry of the $Dy^{III}$ ions was esti-

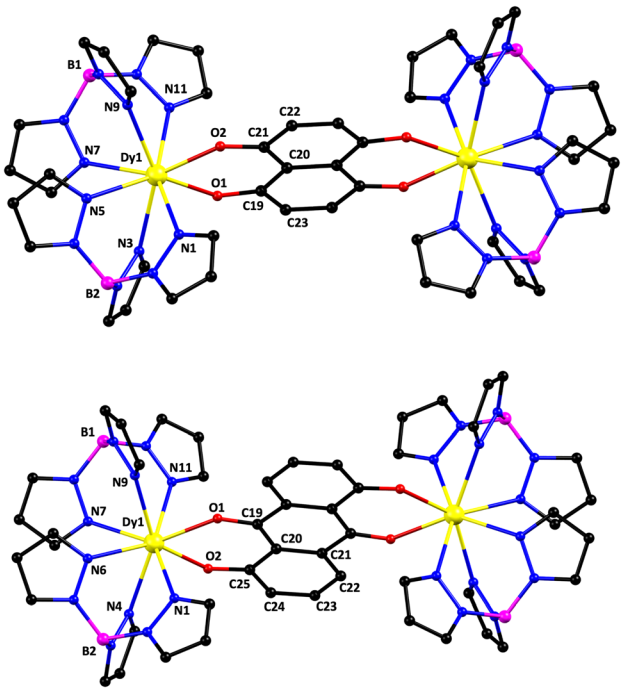


**Fig. 1** Partially labeled representation of **1** (top) and **2** (bottom). Color Scheme: Dy, yellow; N, blue; C, black; B, magenta; O, red. Hydrogen atoms are omitted for the sake of clarity.

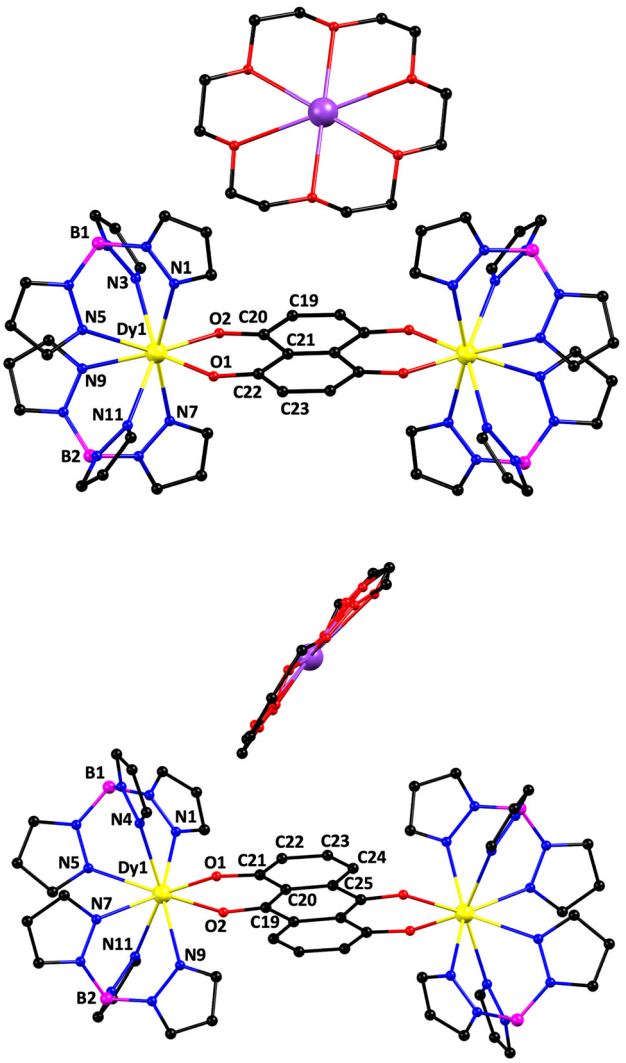


**Fig. 2** Partially labeled representation of **3** (top) and **4** (bottom). Color Scheme: Dy, yellow; N, blue; C, black; B, magenta; O, red; K, purple. Hydrogen atoms are omitted for the sake of clarity.

mated using the SHAPE[60] program and found to be distorted square antiprismatic in both compounds (CShM = 0.99 and 0.76, respectively; Table S2). The metal ions are almost in the same plane with the bridging ligand (0.033 Å) in **1**, while in **2** the $Dy^{III}$ ions are displaced by 0.123 Å above/below the mean plane of the planar $dhaq^{2-}$ ligand. The intramolecular Dy···Dy separation is 9.078 Å in **1** and 9.441 Å in **2**. To the best of our knowledge, compounds **1** and **2** are the first examples of lanthanide complexes bearing the $dhnq^{2-}$ and $dhaq^{2-}$ ligands.

Chemical reduction of compounds **1** and **2** with one equivalent of $KC_8$ in THF followed by the addition of 18-crown-6 yielded dark green solutions which were layered with $Et_2O$ to afford dark green crystals of the one electron reduced species **3** and **4**, $\{K(18\text{-crown-6})\}[Dy_2(L^{\bullet})(Tp)_4]$ [$L^{\bullet}$ = $dhnq^{3\bullet-}$ (**3**) and $dhaq^{3\bullet-}$ (**4**)], in 45–55% yields.

Complex **3** crystallizes in the triclinic space group $P\bar{1}$, and complex **4** crystallizes in the monoclinic space group $C2/c$. In each case (Fig. 2), the asymmetric unit consists of a half-molecule of the anionic complex $[Dy_2(L^{\bullet})(Tp)_4]^-$ [$L^{\bullet}$ = $dhnq^{3\bullet-}$ (**3**) and $dhaq^{3\bullet-}$ (**4**)], one half of the $\{K(18\text{-crown-6})\}^+$ counter cation, and a THF solvent molecule. The anions in **3** and **4** exhibit structures similar to those observed in **1** and **2**. The $Dy^{III}$ ions in **3** and **4** are also 8-coordinate, possessing the same $\{N_6O_2\}$ coordination environment. In the case of **3**, the metal centers exhibit square antiprismatic geometry, while in **4**, the coordination geometry of the $Dy^{III}$ ions is best described as distorted triangular dodecahedral (Table S2). The average Dy–O distances are 2.207 Å and 2.208 Å in **3** and **4**, respectively. The average Dy–N bond distance is similar in both compounds (2.557 Å in **3**, and 2.539 Å in **4**). The $[Dy(Tp)_2]^+$ moieties exhibit B–Dy–B angles comparable to those observed for the unreduced analogues (122.3° in **3** and 127.0° in **4**). The radical bridging ligands $dhnq^{3\bullet-}$ and $dhaq^{3\bullet-}$ adopt the same binding mode as their diamagnetic counterparts, with similar bite angles (74.9° and 75.5° for **3** and **4**, respectively) and bite distances of the six-member chelate ring (2.683 Å and 2.703 Å, for **3** and **4**, respectively). The metal ions are displaced by 0.115 Å or 0.153 Å above/below the mean plane of the bridging $dhnq^{3\bullet-}$ or $dhaq^{3\bullet-}$ ligand for **3** and **4**, respectively. The intramolecular Dy···Dy separation is 9.008 Å in **3** and 9.316 Å in **4**.

While there are several structural similarities among complexes **1–4**, a detailed comparison of the bond distances in **1–4** has revealed significant differences and provided crucial insight into the oxidation state of the dhnq and dhaq bridging ligands. A comparison of **1** with **3** and **2** with **4** reveals a net increase in the average C–O bond order by 1.7% and 2.3%

**Table 1** Selected structural parameters: average distances (Å), angles (°), and coordination geometries for the 8-coordinate $Dy^{III}$ ions in compounds **1**·6$CH_2Cl_2$, **2**·6$CH_2Cl_2$, **3**·2THF and **4**·2THF

| | Diamagnetic ligand | | Radical ligand | |
|---|---|---|---|---|
| Complex | **1**·6$CH_2Cl_2$ | **2**·6$CH_2Cl_2$ | **3** BHF | **4** BHF |
| B–Dy–B angle | 125.0 | 128.3 | 122.3 | 127.0 |
| Dy–L bite angle | 72.9 | 73.0 | 74.9 | 75.5 |
| Dy bite distance | 2.639 | 2.698 | 2.683 | 2.703 |
| Dy–O distance | 2.267 | 2.267 | 2.207 | 2.208 |
| Dy–N distance | 2.514 | 2.508 | 2.557 | 2.539 |
| C–O distance | 1.284 | 1.272 | 1.306 | 1.302 |
| Dy–L plane distance | 0.033 | 0.123 | 0.115 | 0.153 |
| Dy–Dy intramolecular distance | 9.078 | 9.441 | 9.008 | 9.316 |
| Dy coordination geometry | Square antiprismatic | Square antiprismatic | Square antiprismatic | Triangular dodecahedral |

(Table 1), respectively, indicative of the presence of an additional electron in the molecular orbitals of the ligands. Upon reduction, the average C–C bond distances remain unchanged within error, but it is worth noting that these values are influenced by the presence of crystallographic inversion symmetry, which complicates their interpretation.[61] Furthermore, in both **3** and **4**, there is a notable 2.6% decrease in the average Dy–O bond distance. This decrease signifies a stronger metal–ligand interaction, in line with the enhanced donating capability of the reduced $dhnq^{3\bullet-}$ or $dhaq^{3\bullet-}$ ligands compared to their dianionic counterparts. To the best of our knowledge, compounds **3** and **4** are the first examples of lanthanide radical-bridged complexes bearing the $dhnq^{3\bullet-}$ and $dhaq^{3\bullet-}$ ligands.

## Magnetic studies

### Static properties

Direct current (dc) magnetic susceptibility measurements were conducted on powdered polycrystalline samples of **1–4** using a magnetic field of 0.1 T over a temperature range of 2–300 K. The data are displayed as $\chi_M T$ *versus* $T$ plots in Fig. 3. For compounds **1** and **2**, the experimental $\chi_M T$ values (28.20 and 28.03 $cm^3$ K $mol^{-1}$, for **1** and **2**, respectively) at 300 K are in excellent agreement with the theoretical value (28.34 $cm^3$ K $mol^{-1}$) expected for two non-interacting $Dy^{III}$ ($^6H_{15/2}$, $S = 5/2$, $L = 5$, $g = 4/3$) ions.[62] Upon cooling, the $\chi_M T$ product for complexes **1** and **2** decreases smoothly from 300 K to a value of 27.00 $cm^3$ K $mol^{-1}$ for **1** and 28.25 $cm^3$ K $mol^{-1}$ for **2** at 100 K. For **1**, a more pronounced decrease in the $\chi_M T$ product is observed below 100 K, reaching a minimum value of 22.67 $cm^3$ K $mol^{-1}$ at 2 K. Compound **2** exhibits a similar trend, but only down to 4 K. Below this temperature, there is a slight increase in $\chi_M T$ for **2**, reaching a value of 26.05 $cm^3$ K $mol^{-1}$ at 2 K. The decrease observed below 100 K, for **1** and **2**, can be attributed to the depopulation of the excited Stark sublevels of the $Dy^{III}$ ions and/or weak antiferromagnetic interactions between the metal centers, while the slight low-temperature increase observed for **2** may indicate weak ferromagnetic coupling between intramolecular $Dy^{III}$ ions.[63]

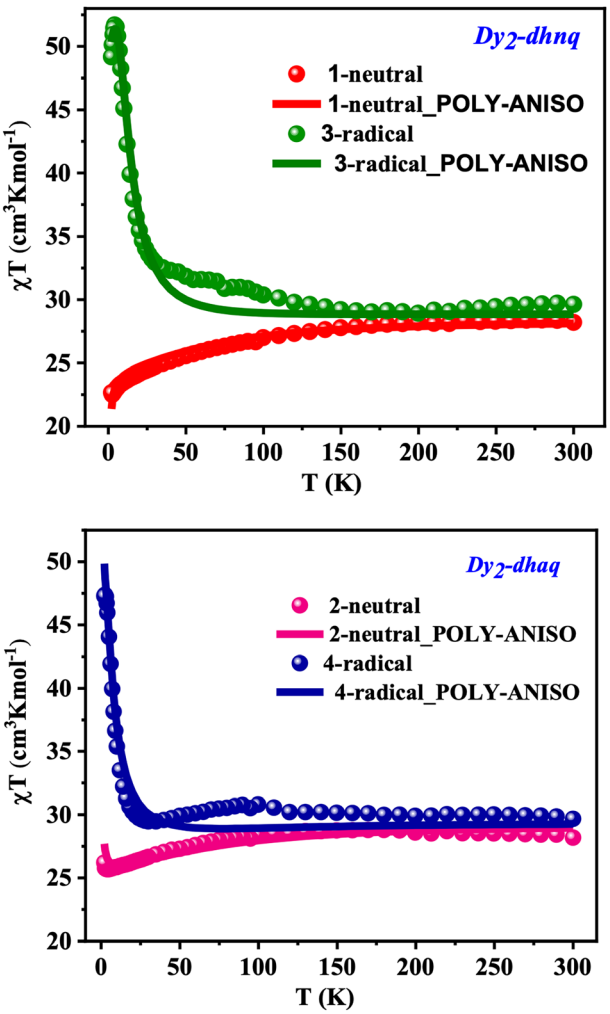


**Fig. 3** Plots of $\chi_M T$ *versus* $T$ for **1–4**.

A pronounced disparity in magnetic behavior is observed for the radical-bridged analogues **3** and **4**. In both cases, the experimental $\chi_M T$ values (29.62 $cm^3$ K $mol^{-1}$ for **3**, and 29.67 $cm^3$ K $mol^{-1}$ for **4**) at 300 K are in agreement with the theoretical value (28.72 $cm^3$ K $mol^{-1}$) predicted for two non-interacting $Dy^{III}$ ($^6H_{15/2}$, $S = 5/2$, $L = 5$, $g = 4/3$) ions and an $S =$

1/2 organic radical. For **3**, the $\chi_M T$ product exhibits a slight increase as the temperature is decreased, reaching a value of 32.31 $cm^3$ K $mol^{-1}$ at 28 K. Below this temperature, the $\chi_M T$ product increases more sharply, peaking at a value of 51.70 $cm^3$ K $mol^{-1}$ at 4 K. After reaching this maximum, the $\chi_M T$ product falls to a minimum value of 49.17 $cm^3$ K $mol^{-1}$ as the temperature is lowered to 2 K. The $\chi_M T$ product for **4** decreases slightly to a minimum value of 29.53 $cm^3$ K $mol^{-1}$ at 28 K before increasing to a maximum value of 47.28 $cm^3$ K $mol^{-1}$ at 2 K. The sudden increase of $\chi_M T$ product observed below 28 K, for **3** and **4**, can be attributed to the spin alignment of the $Dy^{III}$ ions induced by the strong magnetic interactions between the $dhnq^{3\bullet-}$ or $dhaq^{3\bullet-}$ radicals and the metal centers. These results align with observations made for other radical-bridged lanthanide complexes. The decrease in $\chi_M T$ at lower temperatures for **3** can be ascribed to magnetic blocking.[41,42]

Field-dependent magnetization measurements were performed on **1–4** at 2, 5, and 7 K temperatures over the range of 0–7 T (Fig. S1–S4). For **1–4**, magnetization shows a relatively rapid increase at low fields without reaching saturation at ~7 T, which indicates significant magnetic anisotropy. Furthermore, the observed magnetization values for the reduced complexes, **3** and **4**, at 2 K and 7 T are slightly lower compared to those of compounds **1** and **2**. This difference is more likely a consequence of magnetic anisotropy effects, rather than of antiferromagnetic coupling between the metal ions and radical ligands in **3** and **4**.

## Dynamic properties

Alternating current (ac) magnetic susceptibility measurements were conducted using a 2 Oe ac field to investigate the magnetic dynamics of **1–4**. Compounds **1** and **2**, which feature the diamagnetic form of the $dhnq^{2-}$ and $dhaq^{2-}$ ligands, respectively, displayed both in-phase ($\chi'$) and out-of-phase ($\chi''$) ac susceptibility signals that are frequency and temperature dependent in the absence of an applied dc field (Fig. S5 and S6).

However, within the frequency range of 1–1000 Hz and temperatures spanning from 2 to 25 K, no maxima were detected in the $\chi''$ signals, suggesting considerable quantum tunnelling of the magnetization (QTM). Additionally, ac susceptibility measurements were performed at various static fields (0–2000 Oe) (Fig. S7 and S8), but they did not improve the SMM properties of **1** and **2**. Due to the pronounced QTM, $U_{eff}$ could not be determined in either case.

In stark contrast, the reduced complexes, **3** and **4**, exhibit out-of-phase ($\chi''$) ac susceptibility peaks that shift to lower frequencies as the temperature decreases, indicative of slow magnetic relaxation (Fig. 4a,b, and Fig. S9–S14). The experimental data between 1.8–4 K and 1.8–3.6 K, for **3** and **4**, respectively, were used for the construction of the Cole–Cole plots for complexes **3** and **4** (Fig. S11 and S14). Fitting of the Cole–Cole plots for **3** and **4** using a generalized Debye model[64,65] was performed, allowing for the extraction of the $\tau$ and $\alpha$ parameters. The $\alpha$ values are in the range of 0.19–0.08 for **3** and 0.17–0.03 for **4**, in accordance with a single temperature-dependent relaxation process. The relaxation times ($\tau$) obtained from the above fitting were plotted *vs.* $1/T$ (Fig. 4c) and were analyzed using the following eqn (1):

$$\tau^{-1} = {\tau_{QTM}}^{-1} + CT^n + {\tau_0}^{-1} \exp\left(-\frac{U_{eff}}{k_B T}\right) \quad (1)$$

where ${\tau_{QTM}}^{-1}$, $CT^n$, and ${\tau_0}^{-1}\exp(-U_{eff}/k_B T)$ represent QTM, Raman, and Orbach relaxation processes, respectively. For **3**, the best fitting gave $U_{eff}$ = 24.17 K, $\tau_0 = 3.00 \times 10^{-8}$ s, $C = 2.53 \times 10^{-2}$ $s^{-1}$ $K^{-6.3}$ and $n$ = 6.3, and for **4** $U_{eff}$ = 16.70 K, $\tau_0 = 4.04 \times 10^{-7}$ s, $C = 1.27 \times 10^{-1}$ $s^{-1}$ $K^{-4.0}$ and $n$ = 4.0.

These findings indicate that the presence of the radical on the ligand in **3** and **4** effectively suppresses the quantum tunnelling of magnetization prevalent in the unreduced compounds **1** and **2**, in accord with other reports for radical-bridged lanthanide complexes. The obtained $U_{eff}$ values for **3** and **4** are generally lower than those reported for most N-donor radical-bridged $Dy_2$ complexes. However, as compared to O-donor radical-bridged $Dy_2$ complexes, the $U_{eff}$ values for **3** and **4** are slightly higher than the value reported for the bromoanilate radical ($U_{eff}$ = 10.4 K, $H_{dc}$ = 0 Oe)[33] and comparable with those reported for the chloroanilate radical ($U_{eff}$ = 31 K), which were measured in the presence of an external field ($H_{dc}$ = 1000 Oe).[32]

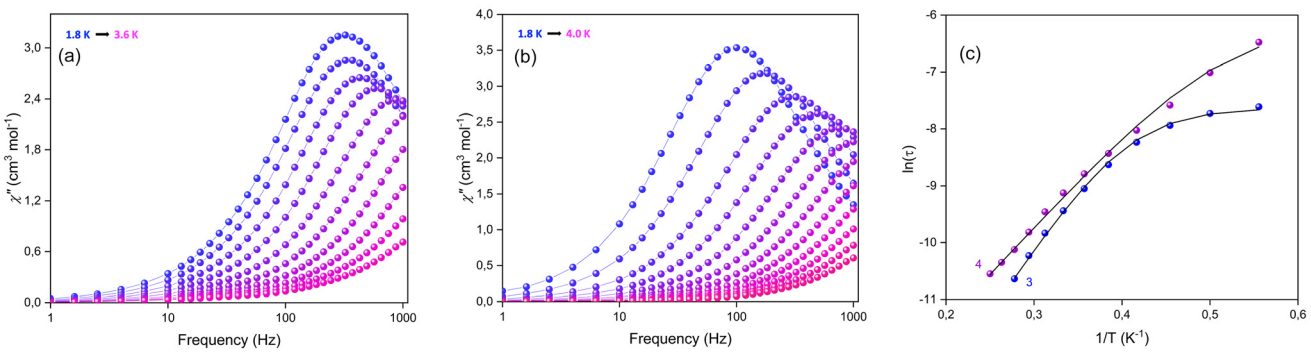


**Fig. 4** Frequency dependence of the out-of-phase ($\chi''$) signals of (a) **3** and (b) under 0 Oe; solid lines are guides for the eye. (c) Comparison of the Arrhenius plots of **3** and **4**. Solid lines highlight the fits to eqn (1) (see the text for the fit parameters).

 

### Computational studies

To investigate the observed magnetic behavior and the nature of magnetic anisotropy of each $Dy^{III}$ center in **1–4**, *ab initio* CASSCF/RASSI/SINGLE_ANISO calculations using the MOLCAS 8.0[66] (see computational details) were performed. The magnetic anisotropy direction of each $Dy^{III}$ ion in **1** and **2** is depicted in Fig. 5 (a similar anisotropy direction is observed in **3** and **4**). The calculated $g_z$ values for both $Dy^{III}$ sites in **1–4** have similar values, signifying the same type of single-ion anisotropy behavior for both $Dy^{III}$ sites (Table 2 and Table S3). Both $Dy^{III}$ ions in **1–4** exhibit small transverse components ($g_x$ and $g_y$) and a strong axial component ($g_z$) in their ground Kramers doublet (KD) states. This suggests a low chance of mixing between the $m_J$ states, which may suppress quantum tunneling of the magnetization (QTM), and supports the presence of optimal Ising-type anisotropy required for slow magnetization relaxation. Thus, at the single-ion level, their capacity to blockade the magnetization is unlikely to happen in the ground KDs, since the $m_J = \pm 15/2$ was found to be the ground state, but it could possibly occur in the excited KDs; this implies that the compounds are likely to show SMM behavior at zero dc field. Although reduction of **1** and **2** to the radical-bridged analogues **3** and **4** introduces modest changes in Dy–O distances (and coordination geometry in **4**), CASSCF/RASSI/SINGLE_ANISO calculations show that the Dy single ion anisotropy remains essentially the same across the series, indicating that the enhanced SMM behavior of the radical-bridged complexes **3** and **4** arises primarily from Dy–radical exchange, with coordination changes acting only as a secondary tuner.

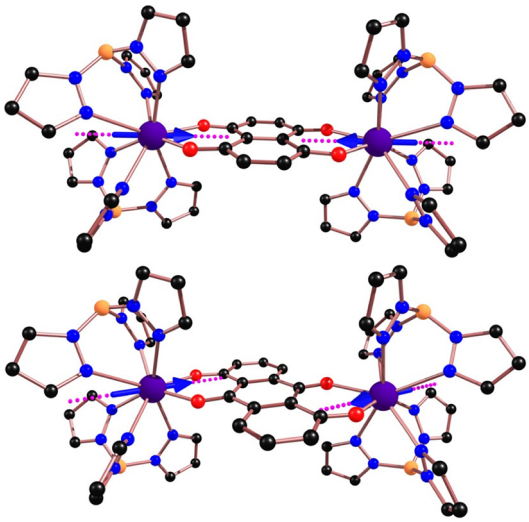

**Fig. 5** Orientations of the local magnetic moments in the ground doublet of each $Dy^{III}$ center in (top) **1** and (bottom) **2**. The blue arrows show the magnetic anisotropy directions of $Dy^{III}$ ions in the ground states. Similar magnetic anisotropy directions were observed for their respective radical-bridged complexes **3** and **4**.

In **1** and **2**, the ground state $g_{zz}$ axis aligns with the O-atoms of the $dhnq^{2-}$ and $dhaq^{2-}$ ligands (see Fig. 5). This is likely owing to the shorter Dy–O (avg.) bond lengths (~2.27 Å in **1** and ~2.25 Å in **2**) of $dhnq^{2-}$ and $dhaq^{2-}$ ligands compared to the longer Dy–N distances (~2.5 Å) of Tp ligands. The oblate electron density of the $Dy^{III}$ ion induces the $g_{zz}$ axis to preferentially align in the same plane towards the shortest Dy–O bond (O atom of $dhnq^{2-}$ and $dhaq^{2-}$ ligands), avoiding significant electrostatic repulsion with the other coordinated atoms, resulting in a greater ground-first excited state gap in all complexes. Similar magnetic anisotropy directions have been observed for **3** and **4**, as shown in Fig. 5.

The computed energies of the eight low-lying KDs (Table 2) for both $Dy^{III}$ sites have the same energy values, a reflection of the fact that they are symmetrically equivalent[67] and are found to span an energy gap of 641.6, 697.3, 740.2, and 740.7 $cm^{-1}$ for **1–4**, respectively. To validate the calculated energy barriers, we developed relaxation mechanisms for magnetization blockade for both $Dy^{III}$ sites in **1–4** (Fig. 6 and Fig. S15). The ground state KDs of both $Dy^{III}$ sites in **1–4** have small QTM ($0.02\mu_B$ for **1**, $0.006\mu_B$ for **2**, $0.03\mu_B$ for **3**, and $0.02\mu_B$ for **4**), hence, it allows the magnetization to relax *via* higher excited states. The Crystal-Field (CF, $B_k^q$) parameters explain the QTM probability of ground-state KDs. The computed CF parameters for **1–4** are listed in Table S5. In both $Dy^{III}$ sites in **1–4**, significant axial terms (in which $q = 0$ and $k = 2, 4, 6$) are computed compared to non-axial terms (in which $q \neq 0$ and $k = 2, 4, 6$), especially

**Table 2** *Ab initio* computed energies of the lowest Kramers Doublets (KDs) and ground-state *g*-tensors of each $Dy^{III}$ centers in all complexes

| | **1** (dhnq-neutral) | | **2** (dhaq-neutral) | | **3** (dhnq-radical) | | **4** (dhaq-radical) | |
|---|---|---|---|---|---|---|---|---|
| KDs | Dy1 | Dy2 | Dy1 | Dy2 | Dy1 | Dy2 | Dy1 | Dy2 |
| 1 | 0.0 | 0.0 | 0.0 | 0.0 | 0.0 | 0.0 | 0.0 | 0.0 |
| 2 | 148.1 | 148.1 | 149.7 | 149.7 | 154.4 | 154.4 | 157.8 | 157.8 |
| 3 | 195.4 | 195.4 | 261.9 | 261.8 | 241.4 | 241.4 | 248.6 | 248.6 |
| 4 | 226.1 | 226.1 | 313.6 | 313.6 | 318.9 | 318.9 | 326.2 | 326.3 |
| 5 | 255.7 | 255.7 | 329.7 | 329.7 | 338.8 | 338.8 | 389.9 | 390.0 |
| 6 | 286.7 | 286.7 | 346.4 | 346.4 | 383.3 | 383.3 | 428.3 | 428.4 |
| 7 | 330.5 | 330.5 | 378.7 | 378.7 | 464.8 | 464.8 | 493.1 | 493.2 |
| 8 | 641.6 | 641.6 | 697.3 | 697.3 | 740.2 | 740.2 | 740.7 | 740.7 |
| $g_x$ | 0.0473 | 0.0471 | 0.0138 | 0.0138 | 0.0690 | 0.0688 | 0.0367 | 0.0367 |
| $g_y$ | 0.0867 | 0.0868 | 0.0216 | 0.0217 | 0.0441 | 0.0437 | 0.0691 | 0.0691 |
| $g_z$ | 19.7155 | 19.7162 | 19.7806 | 19.7894 | 19.4401 | 19.4396 | 19.5550 | 19.5653 |

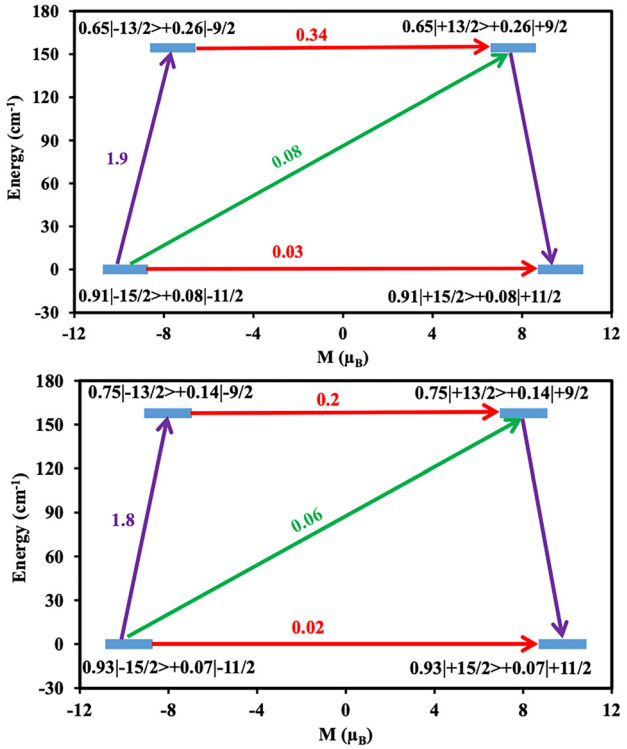


**Fig. 6** *Ab initio* computed magnetization blocking barrier for Dy1 site (same applicable for Dy2 site) in (top) **1**, and (bottom) **2**. The thick blue line indicates the Kramers doublets (KDs) as a function of computed magnetic moment. The red arrows represent the presence of QTM/TA-QTM between the connecting pairs. The green/purple arrows show the possible pathway *via* Orbach/Raman relaxation. The numbers provided at each arrow are the mean absolute value for the corresponding matrix element of the transition magnetic moment.

the axial terms are dominating in $k = 2$ terms, suggesting negligible QTM effects.[67–70] A significant TA-QTM (temperature assisted – QTM) in the first excited states was observed ($0.83\mu_B$ for **1**, $0.1\mu_B$ for **2**, $0.34\mu_B$ for **3**, and $0.2\mu_B$ for **4**), which limits the relaxation of magnetization *via* these states with energy barriers of 148.1, 149.7, 154.2, and 157.8 $cm^{-1}$ (Fig. 6) for **1–4**, respectively. Single-ion calculation results indicate that the radical-bridged complexes **3** and **4** have relatively large energy barriers compared to their respective neutral counterparts (**1** and **2**). However, the conclusive relaxation mechanisms in **1–4** are best understood in terms of exchange-coupled systems.

To understand the overall SMM behavior of **1–4** and the effect of Dy–radical coupling on magnetic relaxation, the exchange coupled states relaxation mechanism was developed by considering the magnetic coupling constants ($J_{exch}$ + $J_{dip}$ = $J_{tot}$) between $Dy^{III}$–rad (only in **3** and **4**) and $Dy^{III}$–$Dy^{III}$, as well as an intermolecular coupling constant $zJ$ using the POLY_ANISO program[71] within the Lines model.[72] The Lines model in POLY_ANISO treats $Dy^{III}$ ions as isotropic spins with $S = 5/2$, which is a simplification used for exchange fitting. The full anisotropy is retained from the *ab initio* CASSCF/RASSI calculations. The computed magnetic coupling constants are tabulated in Table 3. Using the lowest energy states

**Table 3** POLY_ANISO fitted magnetic exchange interactions ($cm^{-1}$, $J_{exch}$ + $J_{dip}$ = $J_{tot}$) in **1–4**

| | $J_{exch}$ | $J_{dip}$ | $J_{tot}$ | $zJ$ |
|---|---|---|---|---|
| $J_{Dy-Dy}$ | | | | |
| **1** (dhnq-neutral) | −0.01 | −0.02 | −0.03 | −0.001 |
| **2** (dhaq-neutral) | 0.005 | −0.015 | −0.01 | 0.01 |
| **3** (dhnq-radical) | 0.58 | −0.03 | 0.55 | −0.002 |
| **4** (dhaq-radical) | 0.62 | −0.02 | 0.6 | 0.008 |
| $J_{Dy-rad}$ | | | | |
| **3** (dhnq-radical) | 4.8 | 0.2 | 5.0 | −0.002 |
| **4** (dhaq-radical) | 1.0 | 0.2 | 1.2 | 0.008 |

of individual $Dy^{III}$ ions and the possible exchange interactions, the *ab initio* calculated magnetic susceptibility data (Fig. 3; solid lines) were computed and are consistent with the experimental data, indicating that the retrieved $J$ values and the $U_{cal}$ parameters are reliable. These calculations reveal a set of exchange split states (Fig. 7), indicating the formation of coupled spin manifolds due to the bridging radicals in **3** and **4**. These states are well isolated from higher excited states and show suppressed QTM in the ground levels for **3** and **4**. The observed $\chi_M T$ product increase at low temperatures and magnetization values (relative to **1** and **2**) is consistent with strong Dy–radical exchange interactions. Thus, the relaxation likely proceeds *via* thermally activated processes within the exchange-coupled ladder, distinct from the tunneling-dominated mechanisms operative in **1** and **2**. The $Dy^{III}$–$Dy^{III}$ interaction is found to be very weakly antiferromagnetic in **1** and **2**, whereas it is found to be ferromagnetic in **3** and **4** and larger in magnitude than that of $J_{Dy-Dy}$. The presence of ferromagnetic $Dy^{III}$–$Dy^{III}$ and $Dy^{III}$–rad interactions in **3** and **4** is attributed to the presence of vacant antibonding orbitals of dhnq and dhaq ligands, which facilitate increased exchange; such an increase in magnitude was previously observed for other $Ln^{III}$–rad complexes.[24,47] The $J_{Dy-rad}$ of **3** is large, with a value of 5.0 $cm^{-1}$ is among the highest ferromagnetic coupling constants reported for a Ln–rad system.[24,27] Ferromagnetic Ln–rad coupling is uncommon, and to our knowledge, it has been observed primarily in systems containing nitronyl nitroxide radicals.[27] We found that the $J_{tot}$ of the $Dy^{III}$–rad interactions in **3** and **4** primarily arises from the $J_{exch}$ (4.8 $cm^{-1}$ for **3** and 1.0 $cm^{-1}$ for **4**) with a comparatively small $J_{dip}$. In general, the $Dy^{III}$–$Dy^{III}$ exchange interaction is expected to be very weak in dinuclear or polynuclear complexes that significantly reduces the energy of low-lying doublet states of $Dy^{III}$ ions, resulting in weak or no SMM behavior in a few Dy-based complexes.[11,73] This hypothesis is clearly operative in the cases of **1** and **2** where the presence of large tunneling gaps (see Tables S6, S7 and Fig. S16) between the ground exchange coupled states (non-Kramer doublet states) allow the magnetization to relax in the ground state itself which suggest no SMM behvaiour for **1** and **2**. However, the presence of ferromagnetic $Dy^{III}$–rad interactions in **3** and **4** produces several low-lying exchange-coupled states and quenches the QTM/TA-QTM in the ground and first excited exchange-coupled states (KDs) to some extent. The TA-QTM becomes larger in the third and fourth exchange-

 

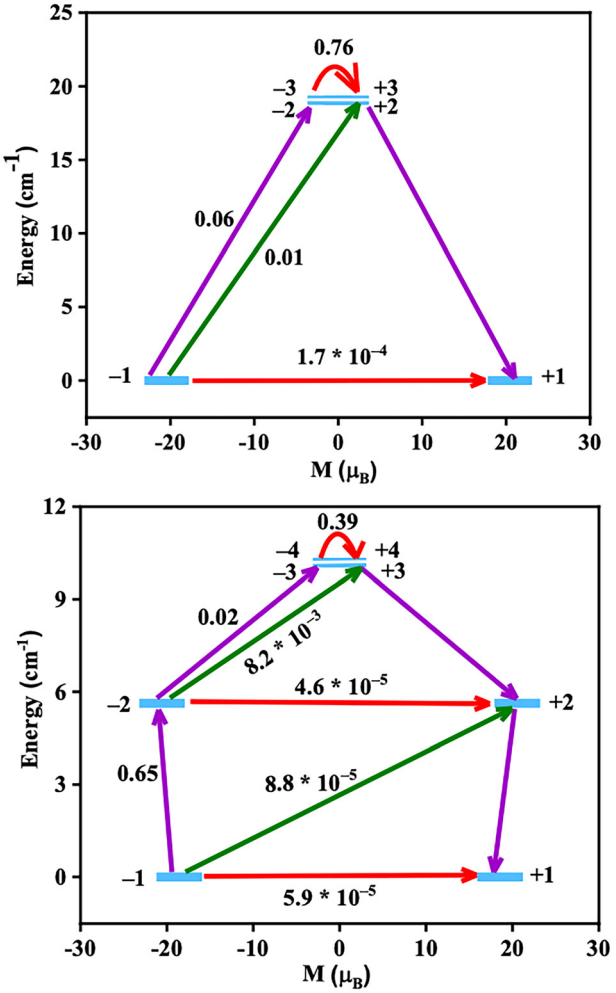


Fig. 7 Low-lying exchange spectra in (top) **3**, and (bottom) **4**. The exchange-coupled states are placed on the diagram according to their magnetic moments (bold blue lines). The red arrows show the QTM/TA-QTM between the connecting states (KDs), while the green/purple arrows show the possible spin–phonon transitions. The numbers provided at each arrow are the mean absolute value for the corresponding matrix element of the transition magnetic moment.

coupled states, which lead to SMM behaviour with an energy barrier of 19.1 $cm^{-1}$ (27.5 K) and 10.2 $cm^{-1}$ (14.7 K), respectively (see Tables S8, S9, and Fig. 7). These $U_{cal}$ parameters are consistent with the experimentally determined barrier of 24.2 K and 16.7 K for **3** and **4**, respectively.

The majority of radical-bridged SMMs utilize anionic radical bridging ligands that align perpendicularly to the primary anisotropy axis of each metal ion.[29,74] For example, in the $[(Cp_2Me_4Tb)_2(\mu\text{-}\eta^2\text{: }\eta^2\text{-}N_2)]$, it is evident that the presence of the radical spin perpendicular to the local magnetic anisotropy axes caused by the Cp* ligands is harmful to the magnetic anisotropy at the $Tb^{III}$ and $Dy^{III}$ sites.[74] Based on these results, it was predicted that it would be advantageous for the spin of the radical bridge to be collinear with the local anisotropy axes, as this arrangement would facilitate ferromagnetic coupling between the metal ions through space and ensure that the anionic radical bridge enhances the existing magnetic anisotropy rather than diminishing it.[4] This theory has been fulfilled in our study: the dianionic or trianionic napthaquinone and anthraquinone ligands, together with improved delocalization of the radical spin on the ligand surface, facilitate a co-parallel orientation between the radical spin and the $g_{zz}$ axis, which promotes the observed ferromagnetic exchange. A similar scenario was reported for the $\{Cp^iPr_5LnI_3LnCp^iPr_5\}$ complex, where the unpaired electron residing in the σ-type Ln–Ln bond is co-parallel to the local magnetic anisotropy axes determined by the $Cp^iPr_5$ ligands, increasing the magnetic anisotropy.[20]

## Conclusions

The first dinuclear $Dy_2$ compounds, **1** and **2**, featuring dianions of the quinoid ligands 5,8-dihydroxy-1,4-naphthoquinone ($dhnqH_2$) and 1,5-dihydroxyanthraquinone ($dhaqH_2$) as bridges, are reported. These molecules were further reduced to produce the radical-bridged $Dy_2$ species, **3** and **4**, containing the $dhnq^{3\bullet-}$ and $dhaq^{3\bullet-}$ radicals, respectively. These are the first, crystallographically characterized, compounds that contain these radical ligands coordinated to a paramagnetic metal ion. Compounds **1**–**4** represent rare examples of pairs of $Dy_2$ compounds with both neutral and radical forms of the same organic bridging ligands, allowing the investigation of the influence of the exchange coupling on the magnetic dynamics. Indeed, magnetic and theoretical studies revealed that in **1** and **2**, the coupling is negligible, resulting in weak SMM behaviour (tails of $\chi''$ signals) and fast magnetic relaxation through QTM. In contrast, placing an additional electron on the bridging ligands in **3** and **4** led to a strong ferromagnetic exchange, which mitigates the occurrence of QTM observed in the unreduced species. Compounds **3** and **4** exhibit maxima of the $\chi''$ signals below 4 K under zero static field, indicative of SMM behaviour. Fitting of the data, considering all possible relaxation pathways, gave energy barriers of 24.17 K and 16.70 K for **3** and **4**, respectively, for the thermally-activated relaxation. The presence of ferromagnetic coupling between the $Dy^{III}$ ions and the radical, with a coupling constant of +5.0 and +1.2 $cm^{-1}$ for **3** and **4**, was confirmed by the Lines model's POLY_ANISO calculations. The computed $U_{cal}$ parameters are in excellent agreement with the experimentally determined barriers. Current efforts are underway to isolate other anisotropic $Ln^{III}$ analogues (*i.e.*, $Ln^{III}$ = $Tb^{III}$, $Er^{III}$, and $Ho^{III}$) as well as to extend this synthetic strategy to the use of other supporting ligands, which are known to promote a strong axial crystal field for oblate $Ln^{III}$ ions.

## Experimental

### Synthetic procedures

For compounds **1** and **2**, all manipulations were performed under aerobic conditions using reagent-grade materials and

solvents as received. For **3** and **4**, all manipulations were carried out under an inert atmosphere of $N_2$ using standard Schlenk and glovebox techniques. Compounds **1** and **2** were dried under vacuum at 100 °C and stored in the glovebox prior to use. Anhydrous THF lacking butylated hydroxytoluene as an inhibitor was purchased from Sigma Aldrich and stored under an inert atmosphere.

**$[Dy_2(dhnq)(Tp)_4]\cdot 6CH_2Cl_2$ ($1\cdot 6CH_2Cl_2$).** To a stirred, beige/brown suspension of $dhnqH_2$ (0.19 g, 1.0 mmol), NaOH (0.08 g, 2.0 mmol), and KTp (1.01 g, 4.0 mmol) in EtOH (80 mL) was added solid $DyCl_3\cdot 6H_2O$ (0.75 g, 2.0 mmol). The resulting dark blue solution was stirred for a further 2 h, after which time the solvent was removed *in vacuo*, and the crude material was extracted using 30 mL of $CH_2Cl_2$. The extract was filtered, and the solution was layered with $Et_2O$ (30 mL). Slow diffusion after 1 day led to blue needles of **1**; these were collected by filtration and washed with $Et_2O$ (3 × 5 mL); the yield was 85%. Upon dryness (under vacuum), the crystalline solid was analyzed as **1**. Anal. calc. for $C_{46}H_{44}N_{24}B_4O_4Dy_2$ (**1**): C, 40.47; H, 3.25; N, 24.62%. Found: C, 40.43; H, 3.21; N, 24.67%. Selected ATR data (Nujol mull, $cm^{-1}$): 1565 (m), 1500 (w), 1403 (w), 1300 (m), 1269 (m), 1213 (m), 1148 (w), 973 (m), 922 (w), 859 (w), 807 (w), 757 (m), 722 (s), 668 (m), 620 (m), 611 (w).

**$[Dy_2(dhaq)(Tp)_4]\cdot 6CH_2Cl_2$ ($2\cdot 6CH_2Cl_2$).** To a stirred, beige/brown suspension of $dhaqH_2$ (0.24 g, 1.0 mmol), NaOH (0.08 g, 2.0 mmol), and KTp (1.01 g, 4.0 mmol) in EtOH (80 mL) was added solid $DyCl_3\cdot 6H_2O$ (0.75 g, 2.0 mmol). The resulting dark red solution was stirred for a further 2 h, after which time the solvent was removed *in vacuo*, and the crude material was extracted using 30 mL of $CH_2Cl_2$. The extract was filtered, and the solution was layered with $Et_2O$ (30 mL). Slow diffusion after 1 day led to red needles of **2**; these were collected by filtration and washed with $Et_2O$ (3 × 5 mL); the yield was 75%. Upon dryness (under vacuum), the crystalline solid was analyzed as **2**. Anal. calc. for $C_{50}H_{46}N_{24}B_4O_4Dy_2$ (**2**): C, 42.43; H, 3.28; N, 23.75%. Found: C, 42.38; H, 3.31; N, 23.79%. Selected ATR data (Nujol mull, $cm^{-1}$): 1733 (w), 1603 (s), 1584 (s), 1617 (s), 1502 (s), 1404 (m), 1300 (s), 1257 (s), 1212 (s), 1199 (m), 1167 (m), 1147 (w), 1120 (s), 1093 (w), 1048 (s), 976 (s), 922 (w), 887 (w), 864 (w), 864 (w), 781 (m), 750 (s), 722 (s), 671 (m), 636 (w), 621 (m), 572 (m), 474 (w).

**{K(18-crown-6)}$[Dy_2(dhnq)(Tp)_4]\cdot 2THF$ ($3\cdot 2THF$).** In a nitrogen-filled glovebox, crystals of $[Dy_2(dhnq)(Tp)_4]$ (**1**) (0.10 g, 0.07 mmol) were dissolved in THF (10 mL) to yield a dark blue solution. Solid $KC_8$ (0.01 g, 0.07 mmol) was then added, and the color of the solution turned dark green. The mixture was stirred at room temperature for 1 h, after which time solid 18-crown-6 (0.04 g, 0.15 mmol) was added and the solution was filtered. The filtrate was layered with $Et_2O$ (10 mL). Slow mixing after 1 day produced dark green platelets of **3**; these were collected by filtration and washed with $Et_2O$ (3 × 5 mL); the yield was 45%. Upon dryness (under vacuum), the crystalline solid was analyzed as **3**. Anal. calc. for $C_{58}H_{68}N_{24}B_4O_{10}KDy_2$ (**3**): C, 41.75; H, 4.11; N, 20.15%. Found: C, 41.79; H, 3.98; N, 20.11%. Selected ATR data (Nujol mull, $cm^{-1}$): 1542 (m), 1495 (s), 1398 (m), 1351 (w), 1300 (s), 1266 (s), 1215 (s), 1199 (m), 1114 (m), 1099 (s), 1043 (s), 972 (m), 953 (s), 920 (w), 894 (w), 832 (m), 806 (w), 774 (s), 752 (s), 722 (s), 667 (m), 623 (m), 533 (w), 499 (w).

**{K(18-crown-6)}$[Dy_2(dhaq)(Tp)_4]\cdot 2THF$ ($4\cdot 2THF$).** In a nitrogen-filled glovebox, crystals of $[Dy_2(dhaq)(Tp)_4]$ (**2**) (0.10 g, 0.07 mmol) were dissolved in THF (10 mL) to yield a dark red solution. Solid $KC_8$ (0.01 g, 0.07 mmol) was then added, and the color of the solution turned dark green. The mixture was stirred at room temperature for 1 h, after which time solid 18-crown-6 (0.04 g, 0.15 mmol) was added, and the solution was filtered. The filtrate was layered with $Et_2O$ (10 mL). Slow diffusion after 1 day led to isolation of dark green plates of **4**; these were collected by filtration and washed with $Et_2O$ (3 × 5 mL); the yield was 55%. Upon dryness (under vacuum), the crystalline solid was analyzed as **4**. Anal. calc. for $C_{70}H_{86}N_{24}B_4O_{10}KDy_2$ (**4**): C, 43.33; H, 4.10; N, 19.56%. Found: C, 43.29; H, 3.06; N, 19.51%. Selected ATR data (Nujol mull, $cm^{-1}$): 1563 (w), 1535 (w), 1349 (m), 1300 (s), 1251 (m), 1198 (m), 1187 (m), 1149 (w), 1108 (s), 1080 (m), 1042 (s), 972 (m), 960 (m), 922 (w), 855 (m), 796 (w), 780 (m), 737 (m), 723 (s), 704 (w), 670 (m), 622 (m), 585 (m), 486 (w).

## Crystallography

Diffraction data for complexes $1\cdot 6CH_2Cl_2$, $2\cdot 6CH_2Cl_2$, $3\cdot 2THF$, and $4\cdot 2THF$ were collected on a Bruker D8 diffractometer (Mo Kα graphite-monochromated radiation, $\lambda = 0.71073$ Å) with the acquisition controlled by the APEX2 software package.[75] The data collection temperature, 150(2) K, was controlled by an Oxford Cryosystems Series 700. Images were processed with the software SAINT+,[76] and absorption effects were corrected with the multi-scan method implemented in SADABS.[77] The structure was solved using SHELXTL incorporated in the Bruker APEX-III software package and refined using the SHELXLE.[78–80] All non-hydrogen atoms were successfully refined using anisotropic displacement parameters. H-atoms bound to carbon atoms were placed at geometrical positions using the suitable HFIX instructions in SHELXL and included in subsequent refinement cycles in riding-motion approximation with isotropic thermal displacement parameters ($U_{iso}$) fixed at the carbon atom to which they are attached. H-atoms associated with the coordinated and non-coordinated MeOH molecules were clearly visible in the difference Fourier maps and included in subsequent refinement stages with the O–H distances restrained to 0.85(2) Å and by using a riding-motion approximation with an isotropic thermal displacement parameter ($U_{iso}$) fixed at 1.5 × $U_{eq}$ of the parent O-atom.

Figures of the structures were created using Mercury[81] and Diamond[82] software packages. The unit cell parameters, structure solution, and refinement details of $1\cdot 6CH_2Cl_2$, $2\cdot 6CH_2Cl_2$, $3\cdot 2THF$, and $4\cdot 2THF$ are summarized in Table S1. Further crystallographic details can be found in the corresponding CIF files provided in the SI.

## Physical studies

Infrared spectra were obtained using a Nicolet Nexus 470 FT-IR Spectrometer. Elemental analyses were performed by Atlantic

 

Microlabs, Inc., Norcross, GA. Variable-temperature direct current (dc) and alternating current (ac) magnetic susceptibility data were collected on a Quantum Design MPMS-XL SQUID magnetometer equipped with a 7 T magnet and operating in the 2–300 K range. The diamagnetic contribution of the polypropylene bag used to hold the sample was subtracted from the raw data. Pascal's constants[83] were used to estimate the diamagnetic corrections, which were subtracted from the experimental susceptibilities to give the molar paramagnetic susceptibilities ($\chi_M$). Note: All physicochemical characterizations, except X-ray crystallography, were performed on dried samples. Lattice solvents were removed during this process, and elemental analysis confirmed the desolvated forms of the compounds **1–4**.

### Computational details

Using MOLCAS 8.0,[84] *ab initio* calculations were performed on the $Dy^{III}$ ions using their crystal structures. The anisotropy of a single $Dy^{III}$ ion in all complexes was computed using the X-ray structure and by substituting a diamagnetic $Lu^{III}$ ion for the nearby $Dy^{III}$ ion. The presence of radical spins of $dhnq^{3\bullet-}$ and $dhaq^{3\bullet-}$ ligands in **3** and **4** was considered as point charges while performing the calculations. Relativistic effects were taken into account based on the Douglas–Kroll Hamiltonian.[85] The spin-free eigenstates are achieved by the Complete Active Space Self-Consistent Field (CASSCF) method.[86] The basis sets were taken from the ANO-RCC library for the calculations. We employed the [ANO-RCC···8s7p5d3f2g1h.] basis set[87] for $Dy^{III}$ atoms, the [ANO-RCC···3s2p.] basis set for B and C atoms, the [ANO-RCC···2s.] basis set for H atoms, the [ANO-RCC···3s2p1d.] basis set for O and N atoms, and the [ANO-RCC···7s6p4d2f.] basis set for the Lu atom. In the first step, we ran a guessorb calculation using a Seward module to create the starting guess orbitals. Here, we included nine electrons across seven 4f orbitals of the $Dy^{III}$ ion. Then, using these guess orbitals, we chose the active space based on the number of active electrons in the number of active orbitals and carried out the SA-CASSCF calculations. Here, the Configuration Interaction (CI) procedure was computed for $Dy^{III}$ ions, and we considered twenty-one sextet excited states, two hundred and twenty-four quartet excited states, and four hundred and eighty doublet excited states in the calculations to compute the anisotropy. All the excited states corresponding to each multiplet of ions were computed in the CASSCF module. After computing these excited states, we mixed all the low-lying excited states (<50000 $cm^{-1}$) using the RASSI-SO[88] module to calculate the spin–orbit coupled states. Moreover, these computed SO states were considered in the SINGLE_ANISO[89] program to compute the *g*-tensors. The *g*-tensors for the Kramers doublets of $Dy^{III}$ were computed based on the pseudospin $S = \frac{1}{2}$ formalism.[89] Crystal-field (CF) parameters have been extracted using the SINGLE_ANISO code, as implemented in MOLCAS 8.0. The CF parameters for all complexes were analyzed for deeper insight into the mechanism of magnetic relaxation. The corresponding crystal field Hamiltonian is given in the equation:

$$\hat{H}_{CF} = \sum \sum_{k=-q}^{q} B_k^q \tilde{O}_k^q \quad (2)$$

where $B_k^q$ is the crystal field parameter and $O_k^q$ is Steven's operator.

The exchange/dipolar interactions for $Dy^{III}$–radical and $Dy^{III}$–$Dy^{III}$ were computed by fitting the experimental data using the POLY_ANISO program.[71] The exchange Hamiltonian adapted for all complexes is shown below.

$$\hat{H}_{ex} = -\sum_{i=1}^{2} J_i S_i S_{i+1} \quad (3)$$

(here $J_i = J_i^{dipolar} + J_i^{exch}$; *i.e.*, $J_i$ is the total magnetic interaction in the combination of calculated $J_i^{dipolar}$ and fitted $J_i^{exch}$ parameters; this describes the interaction between all the neighboring metal centers.)

The low-lying exchange spectra were derived for all complexes using these exchange interactions, and by considering six KDs of each Dy(III) ion, and an additional doublet state of radical spin was considered for complexes **3** and **4**.

## Conflicts of interest

There are no conflicts to declare.

## Data availability

The data supporting this article have been included as part of the SI: crystallographic/refinement tables, dc/ac magnetic measurements and analyses, and *ab initio* computational figures and tables for complexes **1–4**) have been included as part of the SI. See DOI: **https://doi.org/10.1039/d5qi01477h**.

CCDC 2471757–2471760 (**1–4**) contain the supplementary crystallographic data for this paper.[90a–d]

## Acknowledgements

We gratefully acknowledge support for this work by the National Science Foundation (CHE-1808779) and the Robert A. Welch Foundation (Grant A-1449). The SQUID magnetometer used was purchased with funds provided by the Texas A&M University Vice President of Research. We are grateful to the HPRC at Texas A&M for the computing resources. D. I. A. acknowledges finance support from the programme "MEDICUS" of the University of Patras. L. C.-S. thanks financial support received from the PT national funds (FCT/MECI, Fundação para a Ciência e Tecnologia/Ministério da Educação, Ciência e Inovação) through the project UID/50006 – Laboratório Associado para a Química Verde – Tecnologias e Processos Limpos.

## References

1 R. Bagai and G. Christou, The Drosophila of single-molecule magnetism: [Mn12O12(O2CR)16($H_2O$)4], *Chem. Soc. Rev.*, 2009, **38**, 1011–1026.
2 A. Zabala-Lekuona, J. M. Seco and E. Colacio, Single-Molecule Magnets: From Mn12-ac to dysprosium metallocenes, a travel in time, *Coord. Chem. Rev.*, 2021, **441**, 213984.
3 E. Coronado, Molecular magnetism: from chemical design to spin control in molecules, materials and devices, *Nat. Rev. Mater.*, 2020, **5**, 87–104.
4 N. F. Chilton, Molecular Magnetism, *Annu. Rev. Mater. Res.*, 2022, **52**, 79–101.
5 R. Sessoli, D. Gatteschi, A. Caneschi and M. A. Novak, Magnetic bistability in a metal-ion cluster, *Nature*, 1993, **365**, 141.
6 L. Bogani and W. Wernsdorfer, Molecular spintronics using single-molecule magnets, *Nat. Mater.*, 2008, **7**, 179.
7 E. Moreno-Pineda, C. Godfrin, F. Balestro, W. Wernsdorfer and M. Ruben, Molecular spin qudits for quantum algorithms, *Chem. Soc. Rev.*, 2018, **47**, 501–513.
8 R. Sessoli and A. K. Powell, Strategies towards single molecule magnets based on lanthanide ions, *Coord. Chem. Rev.*, 2009, **253**, 2328–2341.
9 L. Sorace, C. Benelli and D. Gatteschi, Lanthanides in molecular magnetism: old tools in a new field, *Chem. Soc. Rev.*, 2011, **40**, 3092–3104.
10 J. D. Rinehart and J. R. Long, Exploiting single-ion anisotropy in the design of f-element single-molecule magnets, *Chem. Sci.*, 2011, **2**, 2078–2085.
11 D. N. Woodruff, R. E. P. Winpenny and R. A. Layfield, Lanthanide Single-Molecule Magnets, *Chem. Rev.*, 2013, **113**, 5110–5148.
12 N. Ishikawa, M. Sugita, T. Ishikawa, S.-y. Koshihara and Y. Kaizu, Lanthanide Double-Decker Complexes Functioning as Magnets at the Single-Molecular Level, *J. Am. Chem. Soc.*, 2003, **125**, 8694–8695.
13 Y.-S. Ding, N. F. Chilton, R. E. P. Winpenny and Y.-Z. Zheng, On Approaching the Limit of Molecular Magnetic Anisotropy: A Near-Perfect Pentagonal Bipyramidal Dysprosium(III) Single-Molecule Magnet, *Angew. Chem., Int. Ed.*, 2016, **55**, 16071–16074.
14 A. K. Bar, P. Kalita, M. K. Singh, G. Rajaraman and V. Chandrasekhar, Low-coordinate mononuclear lanthanide complexes as molecular nanomagnets, *Coord. Chem. Rev.*, 2018, **367**, 163–216.
15 B. M. Day, F.-S. Guo and R. A. Layfield, Cyclopentadienyl Ligands in Lanthanide Single-Molecule Magnets: One Ring To Rule Them All?, *Acc. Chem. Res.*, 2018, **51**, 1880–1889.
16 T. G. Ashebr, H. Li, X. Ying, X.-L. Li, C. Zhao, S. Liu and J. Tang, Emerging Trends on Designing High-Performance Dysprosium(III) Single-Molecule Magnets, *ACS Mater. Lett.*, 2022, **4**, 307–319.
17 F.-S. Guo, B. M. Day, Y.-C. Chen, M.-L. Tong, A. Mansikkamäki and R. A. Layfield, A Dysprosium Metallocene Single-Molecule Magnet Functioning at the Axial Limit, *Angew. Chem., Int. Ed.*, 2017, **56**, 11445–11449.
18 C. A. P. Goodwin, F. Ortu, D. Reta, N. F. Chilton and D. P. Mills, Molecular magnetic hysteresis at 60 kelvin in dysprosocenium, *Nature*, 2017, **548**, 439–442.
19 F.-S. Guo, B. M. Day, Y.-C. Chen, M.-L. Tong, A. Mansikkamäki and R. A. Layfield, Magnetic hysteresis up to 80 kelvin in a dysprosium metallocene single-molecule magnet, *Science*, 2018, **362**, 1400–1403.
20 C. A. Gould, K. R. McClain, D. Reta, J. G. C. Kragskow, D. A. Marchiori, E. Lachman, E.-S. Choi, J. G. Analytis, R. D. Britt, N. F. Chilton, *et al.*, Ultrahard magnetism from mixed-valence dilanthanide complexes with metal-metal bonding, *Science*, 2022, **375**, 198–202.
21 P. Zhang, L. Zhang and J. Tang, Lanthanide single molecule magnets: progress and perspective, *Dalton Trans.*, 2015, **44**, 3923–3929.
22 J. Wang, C.-Y. Sun, Q. Zheng, D.-Q. Wang, Y.-T. Chen, J.-F. Ju, T.-M. Sun, Y. Cui, Y. Ding and Y.-F. Tang, Lanthanide Single-molecule Magnets: Synthetic Strategy, Structures, Properties and Recent Advances, *Chem. – Asian J.*, 2023, **18**, e202201297.
23 A. Caneschi, D. Gatteschi, R. Sessoli and P. Rey, Toward molecular magnets: the metal-radical approach, *Acc. Chem. Res.*, 1989, **22**, 392–398.
24 S. Demir, I.-R. Jeon, J. R. Long and T. D. Harris, Radical ligand-containing single-molecule magnets, *Coord. Chem. Rev.*, 2015, **289–290**, 149–176.
25 Y.-C. Chen and M.-L. Tong, Single-molecule magnets beyond a single lanthanide ion: the art of coupling, *Chem. Sci.*, 2022, **13**, 8716–8726.
26 A. Swain, T. Sharma and G. Rajaraman, Strategies to quench quantum tunneling of magnetization in lanthanide single molecule magnets, *Chem. Commun.*, 2023, **59**, 3206–3228.
27 H.-D. Li, S.-G. Wu and M.-L. Tong, Lanthanide–radical single-molecule magnets: current status and future challenges, *Chem. Commun.*, 2023, **59**, 6159–6170.
28 J. D. Rinehart, M. Fang, W. J. Evans and J. R. Long, A $N_2^{3-}$ Radical-Bridged Terbium Complex Exhibiting Magnetic Hysteresis at 14 K, *J. Am. Chem. Soc.*, 2011, **133**, 14236–14239.
29 S. Demir, J. M. Zadrozny, M. Nippe and J. R. Long, Exchange coupling and magnetic blocking in bipyrimidyl radical-bridged dilanthanide complexes, *J. Am. Chem. Soc.*, 2012, **134**, 18546–18549.
30 S. Demir, M. Nippe, M. I. Gonzalez and J. R. Long, Exchange coupling and magnetic blocking in dilanthanide complexes bridged by the multi-electron redox-active ligand 2,3,5,6-tetra(2-pyridyl)pyrazine, *Chem. Sci.*, 2014, **5**, 4701–4711.
31 F. Benner, L. La Droitte, O. Cador, B. Le Guennic and S. Demir, Magnetic hysteresis and large coercivity in bis-benzimidazole radical-bridged dilanthanide complexes, *Chem. Sci.*, 2023, **14**, 5577–5592.
32 C. A. Gould, L. E. Darago, M. I. Gonzalez, S. Demir and J. R. Long, A trinuclear radical-bridged lanthanide single-

 

molecule magnet, *Angew. Chem., Int. Ed.*, 2017, **56**, 10103–10107.

33 F.-S. Guo and R. A. Layfield, Strong direct exchange coupling and single-molecule magnetism in indigo-bridged lanthanide dimers, *Chem. Commun.*, 2017, **53**, 3130–3133.

34 N. Mavragani, A. A. Kitos, J. L. Brusso and M. Murugesu, Enhancing magnetic communication between metal centres: the role of s-tetrazine based radicals as ligands, *Chem. – Eur. J.*, 2021, **27**, 5091–5106.

35 N. Mavragani, D. Errulat, D. A. Gálico, A. A. Kitos, A. Mansikkamäki and M. Murugesu, Radical-bridged $Ln_4$ metallocene complexes with strong magnetic coupling and a large coercive field, *Angew. Chem., Int. Ed.*, 2021, **60**, 24206–24213.

36 B. S. Dolinar, S. Gómez-Coca, D. I. Alexandropoulos and K. R. Dunbar, An air stable radical-bridged dysprosium single molecule magnet and its neutral counterpart: redox switching of magnetic relaxation dynamics, *Chem. Commun.*, 2017, **53**, 2283–2286.

37 B. S. Dolinar, D. I. Alexandropoulos, K. R. Vignesh, T. A. James and K. R. Dunbar, Lanthanide triangles supported by radical bridging ligands, *J. Am. Chem. Soc.*, 2018, **140**, 908–911.

38 J. A. DeGayner, I.-R. Jeon and T. D. Harris, A series of tetraazalene radical-bridged $M_2$ (M = CrIII, MnII, FeII, CoII) complexes with strong magnetic exchange coupling, *Chem. Sci.*, 2015, **6**, 6639–6648.

39 K. S. Min, A. G. DiPasquale, J. A. Golen, A. L. Rheingold and J. S. Miller, Synthesis, Structure, and Magnetic Properties of Valence Ambiguous Dinuclear Antiferromagnetically Coupled Cobalt and Ferromagnetically Coupled Iron Complexes Containing the Chloranilate(2−) and the Significantly Stronger Coupling Chloranilate(˙3−) Radical Trianion, *J. Am. Chem. Soc.*, 2007, **129**, 2360–2368.

40 C. Hua, J. A. DeGayner and T. D. Harris, Thiosemiquinoid Radical-Bridged $CrIII_2$ Complexes with Strong Magnetic Exchange Coupling, *Inorg. Chem.*, 2019, **58**, 7044–7053.

41 P. Zhang, M. Perfetti, M. Kern, P. P. Hallmen, L. Ungur, S. Lenz, M. R. Ringenberg, W. Frey, H. Stoll, G. Rauhut, *et al.*, Exchange coupling and single molecule magnetism in redox-active tetraoxolene-bridged dilanthanide complexes, *Chem. Sci.*, 2018, **9**, 1221–1230.

42 W. R. Reed, M. A. Dunstan, R. W. Gable, W. Phonsri, K. S. Murray, R. A. Mole and C. Boskovic, Tetraoxolene-bridged rare-earth complexes: a radical-bridged dinuclear Dy single-molecule magnet, *Dalton Trans.*, 2019, **48**, 15635–15645.

43 A. E. Thorarinsdottir, R. Bjornsson and T. D. Harris, Insensitivity of Magnetic Coupling to Ligand Substitution in a Series of Tetraoxolene Radical-Bridged $Fe_2$ Complexes, *Inorg. Chem.*, 2020, **59**, 4634–4649.

44 D. Guo and J. K. McCusker, Spin Exchange Effects on the Physicochemical Properties of Tetraoxolene-Bridged Bimetallic Complexes, *Inorg. Chem.*, 2007, **46**, 3257–3274.

45 H. S. Das, A. K. Das, R. Pattacini, R. Hübner, B. Sarkar and P. Braunstein, First structurally characterized mono- and dinuclear ruthenium complexes derived from zwitterionic quinonoid ligands, *Chem. Commun.*, 2009, 4387–4389.

46 P. B. Chatterjee, K. Bhattacharya, N. Kundu, K.-Y. Choi, R. Clérac and M. Chaudhury, Vanadium-Induced Nucleophilic IPSO Substitutions in a Coordinated Tetrachlorosemiquinone Ring: Formation of the Chloranilate Anion as a Bridging Ligand, *Inorg. Chem.*, 2009, **48**, 804–806.

47 D. Schweinfurth, M. M. Khusniyarov, D. Bubrin, S. Hohloch, C.-Y. Su and B. Sarkar, Tuning Spin–Spin Coupling in Quinonoid-Bridged Dicopper(II) Complexes through Rational Bridge Variation, *Inorg. Chem.*, 2013, **52**, 10332–10339.

48 I.-R. Jeon, J. G. Park, D. J. Xiao and T. D. Harris, An Azophenine Radical-Bridged $Fe_2$ Single-Molecule Magnet with Record Magnetic Exchange Coupling, *J. Am. Chem. Soc.*, 2013, **135**, 16845–16848.

49 D. Schweinfurth, Y. Rechkemmer, S. Hohloch, N. Deibel, I. Peremykin, J. Fiedler, R. Marx, P. Neugebauer, J. van Slageren and B. Sarkar, Redox-Induced Spin-State Switching and Mixed Valency in Quinonoid-Bridged Dicobalt Complexes, *Chem. – Eur. J.*, 2014, **20**, 3475–3486.

50 J. A. DeGayner, K. Wang and T. D. Harris, A Ferric Semiquinoid Single-Chain Magnet via Thermally-Switchable Metal–Ligand Electron Transfer, *J. Am. Chem. Soc.*, 2018, **140**, 6550–6553.

51 A. E. Thorarinsdottir and T. D. Harris, Metal–Organic Framework Magnets, *Chem. Rev.*, 2020, **120**, 8716–8789.

52 T. J. Woods, M. F. Ballesteros-Rivas, S. M. Ostrovsky, A. V. Palii, O. S. Reu, S. I. Klokishner and K. R. Dunbar, Strong Direct Magnetic Coupling in a Dinuclear CoII Tetrazine Radical Single-Molecule Magnet, *Chem. – Eur. J.*, 2015, **21**, 10302–10305.

53 T. J. Woods, H. D. Stout, B. S. Dolinar, K. R. Vignesh, M. F. Ballesteros-Rivas, C. Achim and K. R. Dunbar, Strong Ferromagnetic Exchange Coupling Mediated by a Bridging Tetrazine Radical in a Dinuclear Nickel Complex, *Inorg. Chem.*, 2017, **56**, 12094–12097.

54 D. I. Alexandropoulos, B. S. Dolinar, K. R. Vignesh and K. R. Dunbar, Putting a New Spin on Supramolecular Metallacycles: $Co_3$ Triangle and $Co_4$ Square Bearing Tetrazine-Based Radicals as Bridges, *J. Am. Chem. Soc.*, 2017, **139**, 11040–11043.

55 D. I. Alexandropoulos, K. R. Vignesh, H. Xie and K. R. Dunbar, Quinoxaline radical-bridged transition metal complexes with very strong antiferromagnetic coupling, *Chem. Commun.*, 2020, **56**, 9122–9125.

56 S. Maji, B. Sarkar, S. M. Mobin, J. Fiedler, F. A. Urbanos, R. Jimenez-Aparicio, W. Kaim and G. K. Lahiri, Valence-state alternatives in diastereoisomeric complexes $[(acac)_2Ru(\mu\text{-}QL)Ru(acac)_2]^n$ ($QL^{2-}$ = 1,4-dioxido-9,10-anthraquinone,n = +2, +1, 0, −1, −2), *Inorg. Chem.*, 2008, **47**, 5204–5211.

57 S. Ghumaan, B. Sarkar, S. Maji, V. G. Puranik, J. Fiedler, F. A. Urbanos, R. Jimenez-Aparicio, W. Kaim and G. K. Lahiri, Valence-state analysis through spectroelectrochemistry in a series of quinonoid-bridged diruthenium

complexes $[(acac)_2Ru(\mu\text{-}L)Ru(acac)_2]^n$ (n = +2, +1, 0, −1, −2), *Chem. – Eur. J.*, 2008, **14**, 10816–10828.

58 T. S. Kamatchi, S. Mondal, T. Scherer, M. Bubrin, K. Natarajan and W. Kaim, Near-infrared-absorbing organometallic diruthenium complex intermediates: evidence for bridging anthrasemiquinone formation and against mixed valency, *Chem. – Eur. J.*, 2017, **23**, 17810–17816.

59 K. Herasymchuk, M. Allain, G. A. MacNeil, V. Carré, F. Aubriet, D. B. Leznoff, M. Sallé and S. Goeb, Exciton Coupling in Redox-Active Salen based Self-Assembled Metallacycles, *Chem. – Eur. J.*, 2021, **27**, 16161–16172.

60 S. Alvarez, P. Alemany, D. Casanova, J. Cirera, M. Llunell and D. Avnir, Shape maps and polyhedral interconversion paths in transition metal chemistry, *Coord. Chem. Rev.*, 2005, **249**, 1693–1708.

61 K. Chakarawet, T. D. Harris and J. R. Long, Semiquinone radical-bridged $M_2$ (M = Fe, Co, Ni) complexes with strong magnetic exchange giving rise to slow magnetic relaxation, *Chem. Sci.*, 2020, **11**, 8196–8203.

62 C. Benelli and D. Gatteschi, Magnetism of Lanthanides in Molecular Materials with Transition-Metal Ions and Organic Radicals, *Chem. Rev.*, 2002, **102**, 2369–2388.

63 J. J. Le Roy, J. Cremers, I. A. Thomlinson, M. Slota, W. K. Myers, P. H. Horton, S. J. Coles, H. L. Anderson and L. Bogani, Tailored homo- and hetero-lanthanide porphyrin dimers: a synthetic strategy for integrating multiple spintronic functionalities into a single molecule, *Chem. Sci.*, 2018, **9**, 8474–8481.

64 K. S. Cole and R. H. Cole, Dispersion and Absorption in Dielectrics I. Alternating Current Characteristics, *J. Chem. Phys.*, 1941, **9**, 341–351.

65 S. M. J. Aubin, Z. M. Sun, L. Pardi, J. Krzystek, K. Folting, L. C. Brunel, A. L. Rheingold, G. Christou and D. N. Hendrickson, Reduced Anionic $Mn_{12}$ Molecules with Half-Integer Ground States as Single-Molecule Magnets, *Inorg. Chem.*, 1999, **38**, 5329–5340.

66 F. Aquilante, J. Autschbach, R. K. Carlson, L. F. Chibotaru, M. G. Delcey, L. De Vico, I. F. Galván, N. Ferré, L. M. Frutos, L. Gagliardi, *et al.*, Molcas 8: New capabilities for multiconfigurational quantum chemical calculations across the periodic table, *J. Comput. Chem.*, 2016, **37**, 506–541.

67 K. R. Vignesh, S. K. Langley, K. S. Murray and G. Rajaraman, Quenching the Quantum Tunneling of Magnetization in Heterometallic Octanuclear $\{TMIII_4DyIII_4\}$ (TM = Co and Cr) Single-Molecule Magnets by Modification of the Bridging Ligands and Enhancing the Magnetic Exchange Coupling, *Chem. – Eur. J.*, 2017, **23**, 1654–1666.

68 K. R. Vignesh, S. K. Langley, B. Moubaraki, K. S. Murray and G. Rajaraman, Understanding the Mechanism of Magnetic Relaxation in Pentanuclear $\{MnIVMnIII_2LnIII_2\}$ Single-Molecule Magnets, *Inorg. Chem.*, 2018, **57**, 1158–1170.

69 P. P. Hallmen, C. Köppl, G. Rauhut, H. Stoll and J. van Slageren, Fast and reliable ab initio calculation of crystal field splittings in lanthanide complexes, *J. Chem. Phys.*, 2017, **147**, 164101.

70 Y. Rechkemmer, J. E. Fischer, R. Marx, M. Dörfel, P. Neugebauer, S. Horvath, M. Gysler, T. Brock-Nannestad, W. Frey, M. F. Reid, *et al.*, Comprehensive Spectroscopic Determination of the Crystal Field Splitting in an Erbium Single-Ion Magnet, *J. Am. Chem. Soc.*, 2015, **137**, 13114–13120.

71 L. F. Chibotaru and L. Ungur, *POLY_ANISO program*, University of Leuven, 2006.

72 M. E. Lines, Orbital Angular Momentum in the Theory of Paramagnetic Clusters, *J. Chem. Phys.*, 1971, **55**, 2977–2984.

73 L. Ungur, S. K. Langley, T. N. Hooper, B. Moubaraki, E. K. Brechin, K. S. Murray and L. F. Chibotaru, Net toroidal magnetic moment in the ground state of a $\{Dy_6\}$-triethanolamine ring, *J. Am. Chem. Soc.*, 2012, **134**, 18554–18557.

74 G. T. Nguyen and L. Ungur, The Role of Radical Bridges in Polynuclear Single-Molecule Magnets, *Chem. – Eur. J.*, 2022, **28**, e202200227.

75 APEX2, *Data Collection Software Version 2012.4*, Bruker AXS, Delft, The Netherlands, 2012.

76 SAINT+, *SAINT+, Data Integration Engine v. 7.23a ©*, Bruker AXS, Madison, Wisconsin, USA, 1997–2005.

77 G. M. Sheldrick, *SADABS v.2.01, Bruker/Siemens Area Detector Absorption Correction Program*, Bruker AXS, Madison, Wisconsin, USA, 1998.

78 APEX-III, Bruker AXS Inc., Madison, Wisconsin, USA, 2016.

79 T. Kottke and D. Stalke, Crystal handling at low temperatures, *J. Appl. Crystallogr.*, 1993, **26**, 615–619.

80 C. B. Hubschle, G. M. Sheldrick and B. Dittrich, ShelXle: a Qt graphical user interface for SHELXL, *J. Appl. Crystallogr.*, 2011, **44**, 1281–1284.

81 C. F. Macrae, P. R. Edgington, P. McCabe, E. Pidcock, G. P. Shields, R. Taylor, M. Towler and J. van de Streek, Mercury: visualization and analysis of crystal structures, *J. Appl. Crystallogr.*, 2006, **39**, 453–457.

82 K. Brandenburg and H. Putz, *DIAMOND, Crystal Impact GbR*, Bonn, Germany, 2006.

83 G. A. Bain and J. F. Berry, Diamagnetic Corrections and Pascal's Constants, *J. Chem. Educ.*, 2008, **85**, 532.

84 F. Aquilante, J. Autschbach, R. K. Carlson, L. F. Chibotaru, M. G. Delcey, L. De Vico, I. F. Galván, N. Ferré, L. M. Frutos, L. Gagliardi, *et al.*, MOLCAS 8: New Capabilities for Multiconfigurational Quantum Chemical Calculations across the Periodic Table, *J. Comput. Chem.*, 2016, **37**, 506–541.

85 B. A. Hess, C. M. Marian, U. Wahlgren and O. Gropen, A mean-field spin-orbit method applicable to correlated wavefunctions, *Chem. Phys. Lett.*, 1996, **251**, 365–371.

86 B. O. Roos, P.-Å. Malmqvist, Relativistic quantum chemistry: the multiconfigurational approach, *Phys. Chem. Chem. Phys.*, 2004, **6**, 2919–2927.

87 B. O. Roos, R. Lindh, P.-Å. Malmqvist, V. Veryazov, P.-O. Widmark and A. C. Borin, New Relativistic Atomic Natural Orbital Basis Sets for Lanthanide Atoms with

 

Applications to the Ce Diatom and $LuF_3$, *J. Phys. Chem. A*, 2008, **112**, 11431–11435.

88 P. Å. Malmqvist, B. O. Roos and B. Schimmelpfennig, The restricted active space (RAS) state interaction approach with spin-orbit coupling, *Chem. Phys. Lett.*, 2002, **357**, 230–240.

89 L. F. Chibotaru and L. Ungur, Ab initio calculation of anisotropic magnetic properties of complexes. I. Unique definition of pseudospin Hamiltonians and their derivation, *J. Chem. Phys.*, 2012, **137**, 064112.

90 (*a*) D. I. Alexandropoulos, K. R. Vignesh, L. Cunha-Silva and K. R. Dunbar, CCDC 2471757: Experimental Crystal Structure Determination, 2025, DOI: **10.5517/ccdc.csd.cc2nz23v**; (*b*) D. I. Alexandropoulos, K. R. Vignesh, L. Cunha-Silva and K. R. Dunbar, CCDC 2471758: Experimental Crystal Structure Determination, 2025, DOI: **10.5517/ccdc.csd.cc2nz24w**; (*c*) D. I. Alexandropoulos, K. R. Vignesh, L. Cunha-Silva and K.R. Dunbar, CCDC 2471759: Experimental Crystal Structure Determination, 2025, DOI: **10.5517/ccdc.csd.cc2nz25x**; (*d*) D. I. Alexandropoulos, K. R. Vignesh, L. Cunha-Silva and K.R. Dunbar, CCDC 2471760: Experimental Crystal Structure Determination, 2025, DOI: **10.5517/ccdc.csd.cc2nz26y**.